Lab on a Chip

PAPER

Cite this: *Lab Chip*, 2020, **20**, 3179

An affordable 3D-printed positioner fixture improves the resolution of conventional milling for easy prototyping of acrylic microfluidic devices†

Pablo E. Guevara-Pantoja, [a] Oriana G. Chavez-Pineda, [a] Alberto M. Solis-Serrano, [a] Jose L. Garcia-Cordero *[a] and Gabriel A. Caballero-Robledo *[ab]

Received 26th May 2020,
Accepted 16th July 2020

DOI: 10.1039/d0lc00549e

rsc.li/loc

We present a simple and low-cost positioner fixture to improve the fabrication resolution of acrylic microchannels using conventional milling machines. The positioner fixture is a mechatronic platform that consists of three piezoelectric actuators assembled in a housing made of 3D printer parts. The upper part of the housing is raised by the simultaneous actuation of the piezoelectric elements and by the deformation of 3D-printed hinge-shaped supports. The vertical positioning (*Z*-axis) can be controlled with a resolution of 500 nm and an accuracy of ±1.5 μm; in contrast, conventional milling machines can achieve resolutions of 10 to 35 μm. Through simulations, we found that 3D-printed hinges can deform to reach heights up to 27 μm without suffering any mechanical or structural damage. To demonstrate the capabilities of our fixture, we fabricated microfluidic devices with three weir filters that selectively capture microbeads of 3, 6 and 10 μm. We used a similar weir filter design to implement a bead-based immunoassay. Our positioner fixture increases the resolution of conventional milling machines, thus enabling the fast and easy fabrication of thermoplastic fluidic devices that require finer microstructures in their design.

Introduction

There has been an increased interest in industry and academia to develop microfluidic biomedical devices made of thermoplastics.[1,2] Unlike other materials, thermoplastics are well characterized for biomedical applications; for example, all the accessories that are used in clinical or biochemical laboratories are manufactured in rigid thermoplastics.[3,4] Hot embossing and microinjection are the most widely used techniques for the mass production of plastic devices due to their low cost and high production rates.[1,3] Micromilling does not compete in these aspects, but compared to the aforementioned techniques, it offers prototyping times in the order of minutes or hours instead of days or weeks.[5] Besides, micromilling offers excellent versatility for many materials, whether to manufacture molds for hot-embossing or to pattern microstructures directly on a substrate.[6] Being able to create functional prototypes in a short time can be the difference between marketing a product in a year and being stuck in its development stage.[7] Although other low-cost commercial techniques exist for the fast prototyping of microfluidic devices, such as 3D printing,[8] laser cutting,[9] and die cutting, they lack the resolution to create structures less than 50 μm. Table S1† contains a summary of equipment, costs, resolution and limitations of these techniques.

Micromilling fabrication protocols for thermoplastic microfluidic devices are well established.[6] For example, to create closed channels, different protocols have been described, such as solvent bonding,[10] heat bonding[11] and UV/ozone surface treatment bonding.[12] Also, protocols have been reported for chemical modifications of polymer surfaces in microfluidic systems for different functionalities.[13] Furthermore, our groups have recently reported the manufacturing of valves and pumps integrated into acrylic microfluidic devices.[14]

High-end micromilling machines capable of creating structures with resolutions on the order of microns are commercially available, for example, the TT1-400A of SODICK (3 μm resolution), the 363-S of Microlution (1 μm), or the G4-ULTRA of Atometric (0.1 μm). Nevertheless, because of their high prices (>US $ 100 000), these machines are not easily

[a] *Unidad Monterrey, Centro de Investigación y de Estudios Avanzados del Instituto Politécnico Nacional (Cinvestav), Parque PIIT, Apodaca, Nuevo León 66628, Mexico. E-mail: jlgarciac@cinvestav.mx, gcaballero@cinvestav.mx*

[b] *Université Paris-Saclay, CEA, CNRS, NIMBE, CEA Saclay, 91191, Gif-sur-Yvette Cedex, France*

† Electronic supplementary information (ESI) available. See DOI: 10.1039/d0lc00549e

found in academic laboratories or even in industry. Furthermore, installation and maintenance are expensive, their operation requires trained personnel, and technical support is limited to a handful of countries.

Desktop milling machines with a resolution of 10 to 35 μm can be found for a fraction of the cost (<10 000 USD). For example, Carbide 3D's Nomad 883 can create structures with a resolution of 35 μm, the Othermill V2 features a resolution of 25 μm, and the Roland MDX-40A showcases a resolution of 10 μm. However, this resolution is not enough for some microfluidics applications that require structures smaller than 10 μm. For example, weir microfilters enable several applications such as: bacteria trapping,[15] separation of blood components,[16,17] supporting biosensors with microparticles,[18,19] chromatography columns[20,21] or bead-based immunoassays.[22,23] While it is possible to resort to the equipment and techniques mentioned above to build these devices, it is desirable to develop alternative and affordable equipment that offers micro-resolution within the reach of academic laboratories.

In this paper, we introduce a small and low-cost fixture to increase the resolution of conventional milling machines, allowing the fabrication of microstructures less than 10 μm. Notably, the fixture is small enough to fit on the worktable space of any milling machine. The 3D-printed fixture raises a platform in micron steps while a drilling bit traces a channel on the thermoplastic surface, Fig. 1a. The platform accommodates three piezoelectric actuators fitted in a 3D-printed casing which is assembled from only 3 parts. We developed the electronics to control the actuators, as well as a graphical user interface to monitor the actuator's displacement. Simulations were carried out to estimate the deformations and stresses that undergo some critical areas of the plastic parts. The accuracy in the vertical positioning of the platform was characterized by machining microfluidic channels of different depths. As a proof of concept, we manufactured an acrylic microfluidic device with embedded weirs of different depths: 2, 5 and 9 μm. Finally, using the same weir structures we implemented a sandwich immunoassay employing microbeads.

Materials and methods

Piezoelectric base

Three parts were manufactured using a 3D-printer (Replicator 2, MakerBot) in layers of 100 μm and a 30% infill, Fig. 1b. The pieces were assembled and joined with instant glue

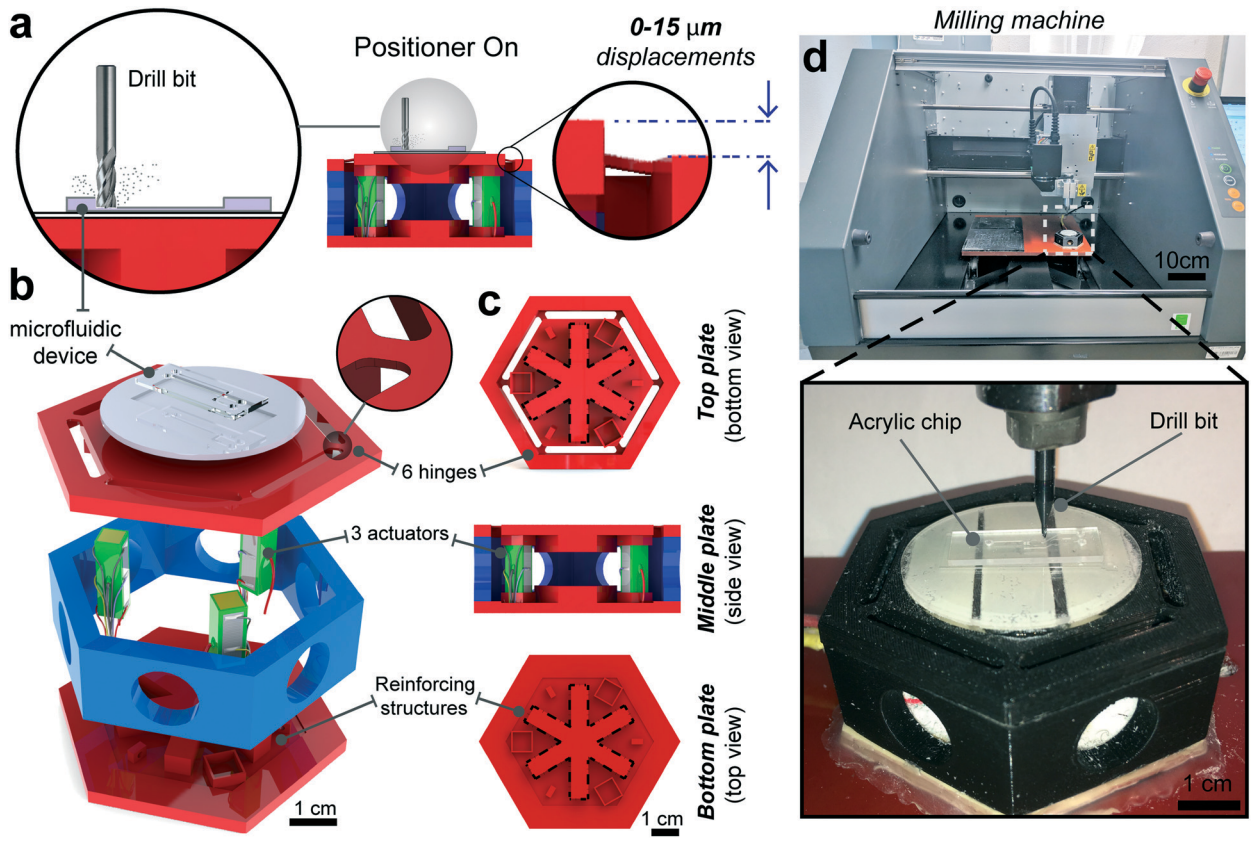

Fig. 1 Design of the vertical positioning fixture. (a) A cross-sectional view of the fixture. Displacement not to scale. The platform can rise to a height of 15 μm in steps of 1 μm by activating 3 piezoelectric actuators simultaneously. (b) Exploded view of the 3D-printed parts that make the fixture; the piezoelectric actuators are shown in green/white color. The closeup shows the design of one of the flexible hinges. The thermoplastic slab to be machined sits on top of the platform. (c) The top and bottom bases have holders for each of the three actuators. The top base features six hinges that connect the core to an outer ring. It is the core that is elevated by the actuators. A cross-sectional view of the assembled platform is shown in the middle. (d) Photograph of the positioning platform (black) mounted inside the worktable of a milling machine.

(Loctite 945), as shown in Fig. 1c. The actuators consisted of three piezoelectric stacks (7 × 6 × 20 mm) with a maximum displacement of 17.5 μm each (Thorlabs, PZS001, USA).

To excite the piezoelectric actuators, a regulated and variable power supply was built to supply voltages from 2.5 to 120 VDC with a maximum current of 500 mA. Fig. S1† shows the schematic of the electronic system. The actuators' displacement was measured by wiring their integrated strain gauge sensors in a resistive Wheatstone bridge configuration. The sensor output signals are read with three analog inputs (Phidgets, 1046, USA) controlled with an interface developed in LabView (National Instruments, USA). The interface displays the value of the output voltage and its corresponding displacement value in micrometers.

The platform is glued (Steren HER-242, Mexico) to the worktable of a milling machine, Fig. 1d (MDX-40A, Roland AG, Germany). Next, a circular piece of acrylic (2 mm thick, 4 cm diam.) is placed on top of the platform and permanently joined with double-sided adhesive tape. Then, a rectangular recess (1.1 × 2.6 cm with a depth of 0.5 mm) is carved out on this acrylic piece and leveled off to ensure a uniform *XY* plane. This recess serves to support workpieces, ensuring that they are always placed in the same position. Workpieces consisting of 1.3 mm thick acrylic slabs (ME303018, Goodfellow, USA) are cut out to a size of 1 cm × 2.5 cm so that they fit in the recess. The acrylic workpieces are temporarily attached to the recess with double-sided adhesive tape (Tuk, 404, Mexico) before milling.

Stress and deformation simulations of the 3D printed hinges

The numerical analysis was performed in COMSOL Multiphysics using the Structural Mechanics Module and its Structural Mechanics interface. The 3D model of the top plate used was imported from SolidWorks as a CAD file. The properties of PLA used in the simulation were the following: density (1.252 g cm^{-3}), Young's modulus (3500 MPa), and Poisson's ratio (0.36). The rest of the model was considered as a free element. The mesh generated was composed of tetrahedral elements with a calibrated size, a maximum and minimum size of 1.4 and 0.014 mm, respectively, and a maximum element growth rate of 1.3. We considered a fixed constraint in the outer ring and applied defined displacements at the locations of the three actuators to evaluate the stress that the hinges undergo. The displacements modeled ranged from 0 to 17 μm (maximum displacement the piezoelectric can reach) in steps of 1 μm. Thus, we performed 18 simulations in total, one for each displacement.

Channel fabrication and depth characterization

To characterize the milling resolution in the *Z*-axis of the piezoelectric platform, straight channels of different depths were milled with a 200 μm diameter square end-mill drill bit (Kyocera, 1600-0080L012) at a spindle speed of 15 000 rpm and a feed rate of 1 mm s^{-1}. The depth of each channel was controlled by varying the excitation voltage of the actuators. The channel depth was measured with a white-light interferometer (smartWLI-basic, GBS mbH) using a Mirau 20× objective.

Chip bonding

The protocol to bind two acrylic slabs consists of exposing the acrylic to an atmosphere saturated with chloroform, created by pouring 1 mL of chloroform into a Petri dish and incubating for 5 min,[10] Fig. S3.† Then, using double-sided adhesive tape (Tuk, 404, Mexico) the acrylic pieces are glued to the lid of the Petri dish and exposed to the chloroform for 1 min. It is essential to leave a gap of 7.5 mm between the surface of the acrylic and the solvent surface. Next, the pieces are incubated for 5 min in an atmosphere without chloroform. Finally, the treated pieces are pressed together at 250 psi and 90 °C for 10 min using a home-made mechanical press.

Fabrication of weir filters

Devices were manufactured in acrylic in two steps: channels less than 10 μm deep were machined using our positioning platform, whereas deeper channels and access holes were machined using the regular milling machine. Because it is difficult to accurately align the surface of the chips with the origin coordinates of the milling machine, the device was leveled off with an end-mill bit, setting the origin of the *Z*-axis on this "new" surface. This method ensures precise positioning of the chip relative to the machine. To avoid losing this calibration due to unprecise movements produced by the proprietary software of the machine, we programmed a series of movements in a numerical control code to perform the rectification of the surface, followed by the machining of the 2, 5 and 9 μm restrictions.

Polystyrene microparticles of 3, 6 and 10 μm (CAT: 18138, 19111 and 17137, respectively, Polysciences Inc. USA) diluted in PBS + Tween-20 0.05% + BSA 1% were used. 100 μL syringes (Hamilton Co., 1710RNR, USA) previously mounted on a syringe pump (Kdscientific, KDS-230, USA), configured in withdrawal mode at a flow rate of 50 μL h^{-1}, were connected to the four outputs of the device, one syringe per output. A syringe tip, which acted as a reservoir and allowed a safe exchange of fluids, was connected to the chip input. Before an experiment, the device was filled with PBS + Tween-20 0.05% + BSA 1% and incubated for 10 min to allow BSA to coat the surfaces and avoid adhesion of the beads to the acrylic walls.[4]

The microchannels were milled with a 200 μm square end-mill bit (Kyocera, 1600-0080L012, USA) while holes were made with an 800 μm square end mill-bit (Kyocera, 1600-0320L048, USA). As mentioned above, the milling of the weir filters was performed using a numerical control code, while for the channels and perforations that require less precision, we used the proprietary software of the manufacturer (Dr Engrave). A flexible tube (1.5 mm outer diameter, AAD04103, Tygon, USA) was glued (HENKEL, RESISTOL 911, USA) to the

inlets and outlets. A spindle speed of 15 000 rpm and a feed rate of 1 mm s^{-1} were used as cutting parameters.

Bead-based immunoassay on a chip

For immunoassays, we designed an acrylic device consisting of 6 microchannels and weir filters. Fabrication details can be found in the ESI.† Streptavidin coated microbeads (mean diameter = 6.7 μm, SVP-60-5, Spherotech Inc.) were washed thrice with 1× ELISA buffer (00420255, eBIOSCIENCE) in PBS by centrifuging at 112*g* for 15 min to remove unbound streptavidin residues and prevent occlusion of the channels. Next, the microbeads were resuspended in 50 μL of ELISA buffer at a concentration of 10^6 beads per mL followed by the addition of biotinylated anti-GFP capture antibodies (ab69313-25, Abcam) at 0.7 μg mL^{-1} (0.6 μL). The resulting suspension was thoroughly mixed on a vortex mixer at 500 rpm (Labnet International, S0200) for 3 h and then incubated overnight at 4 °C. Finally, functionalized beads were washed twice with ELISA buffer and resuspended at 10^6 beads per mL in ELISA buffer with 1% bovine serum albumin (BSA, 10711454001, Sigma).

To perform an immunoassay on a chip, antibody-functionalized microbeads were injected until the weirs were filled. Next, different concentrations of recombinant GFP protein (MB-0752, Vector laboratories) diluted in ELISA (0, 0.1, 1, 10, 100, and 1000 ng ml^{-1}) were flowed in separate microfluidic channels at a flow rate of 1 mL h^{-1} for 10 min using a pressure controller (MFCA-EZ, Fluigent). Then, the microbeads were washed for 5 min with 1× ELISA buffer. Finally, fluorescence micrographs over the filter region were acquired with an inverted fluorescence microscope (AxioObserver, Carl Zeiss) fitted with a 14-bit CCD monochromatic camera (AxioCam 506 mono, Carl Zeiss).

Results and discussion

Platform design

The positioning platform consists of three 3D-printed parts (bottom, middle, and top parts) and three piezoelectric actuators (see Fig. 1). The bottom plate is a solid piece with the shape of a hexagon; to provide greater rigidity and reinforce this solid piece, we included three solid beams that sit on top of this plate. Three rectangular wells are located between these beams to accommodate the actuators. The middle part joins the upper and lower plates and has 6 holes along its sides through which the communication and power cables can exit. The upper plate is similar to the bottom plate, except that it has an outer ring connected to an inner core with six flat hinges. The three piezoelectric actuators are located beneath the inner core and are synchronized to move upwards simultaneously. When the actuators are activated, the inner core rises, and the hinges bulge, while the outer ring remains static. When the actuators are disabled, the hinges return to their original flat shape and therefore the inner core remains at the same height as the outer core. Based on the average size of most microfluidic devices, the working area of the top plate was set to 16 cm^2, but it can be redesigned to accommodate larger devices.

The selected piezoelectric actuators move in steps of 500 nm, with a working distance from 0 to 17.5 μm. It is possible to achieve greater displacements by selecting actuators with higher movements and by modifying the dimensions of the hinges and the plates accordingly.

Stress and deformation calculations

The von Mises yield criterion was used to evaluate whether the hinges suffer permanent deformation or rupture due to the movement of the actuators. The von Mises yield criterion establishes the strain energy density that determines when a material yields under stress, independent of the form of the stress tensor. The material's yield strength or elastic limit (S_y) can be determined by performing simple uniaxial tests. If the von Mises stress is equal or larger than the yield strength, the material suffers permanent deformation or rupture. The elastic limit of PLA has been reported to range between 21 and 98 MPa depending on the printing density, the printing pattern, and their orientation.[24–27] Using these values, it is possible to estimate the failure parameters of the hinges on the top plate.

To calculate the deformations that the hinges undergo during the actuation of the piezoelectric actuators, we carried out 3D finite-element simulations of the top plate considering the mechanical properties of PLA, Fig. 2a. We considered the following parameters: a density of 1250 kg m^{-3}, a Young's modulus of 3.5 GPa, a Poisson ratio of 0.36, and an elastic limit of 21 MPa (extreme case, being more brittle).[27] In our simulations, the outer ring is fixed (no displacement) while imposed displacements are applied at the locations of each of the three actuators, Fig. 2b. The vertical imposed displacements at these points range from 0 to 17.4 μm.

Fig. 2c shows the height profiles of a section of the vertical pate (dashed line in Fig. 2a) for 5 different imposed displacements. As can be readily observed, the inner core elevates in proportion to the displacement imposed at the actuator's locations, reaching the same height. The deformations at the extremes of the plate are expected as the hinges and the outer ring are located at these points. A more pronounced deformation is evident at the opposite side where there is no actuator (vertical dashed line in Fig. 2c) but it does not have any impact on the height reached when machining the device. Nonetheless, these deformations can be corrected by adding extra actuators at each of the free hinges.

Not surprisingly, the hinges experience the largest stresses on the top plate. The graph in Fig. 2d shows that the stress at the hinges is a linear function of the vertical displacement, with higher displacements producing higher stresses. At a maximum displacement of 17.4 μm, the calculated von Misses stress of 13 MPa is lower than the lowest yield strength reported in the literature (Fig. 2e and f). This result implies that the hinges will not be deformed permanently after the actuators are activated and will allow for their continuing use, as we have corroborated. We have used our

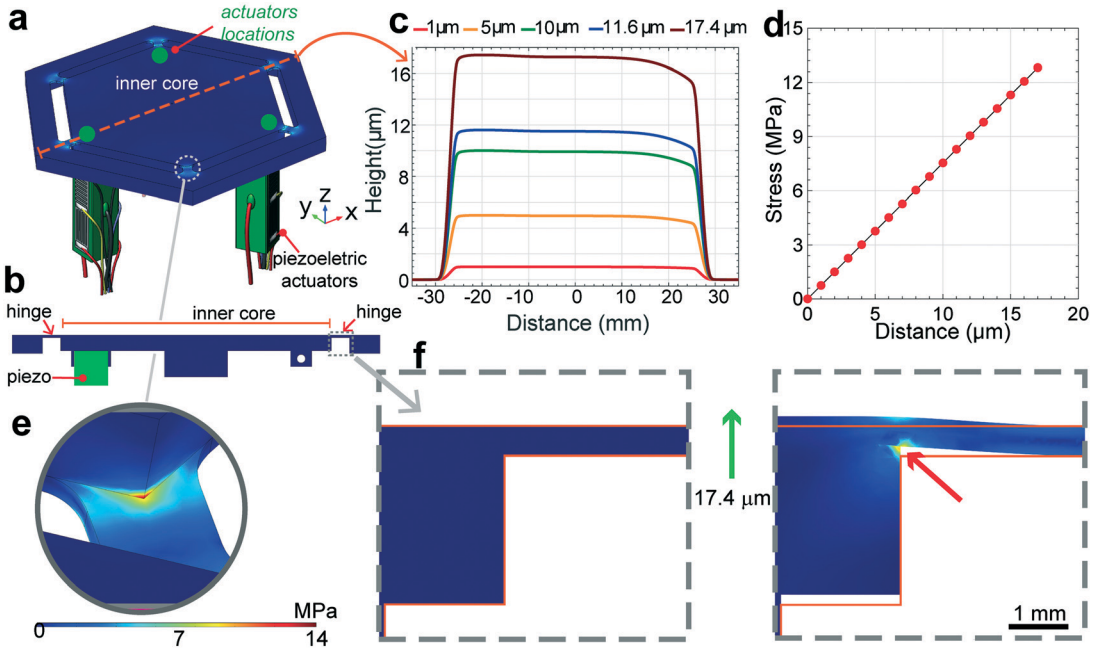

Fig. 2 Mechanical simulations of the top plate. (a) 3D design of the top plate showing the locations of the three actuators (green dots) where vertical displacements are imposed. (b) Cross-sectional view of the top plate indicated by the orange dashed line in a. (c) Simulated height profiles of the top plate for different vertical displacements. (d) Calculated stresses on the plate as a function of its vertical displacement. (e) 3D simulation of the von Mises stress in one of the hinges when the actuators are elevated to a maximum displacement of 17.4 μm. The maximum von Mises stress (red) is found where hinges join the inner core. (f) 2D stress simulations in one of the hinges as it goes from a resting position to a displacement of 17.4 μm. The red arrow points to the corner of the hinge that is subjected to higher stress.

platform for almost one year without any damage or deformation of the hinges so far. With our current design, it should be possible to achieve a maximum vertical distance of 27 μm before reaching the creep limit and undergoing permanent damage.

Vertical positioning accuracy

Without any load, the piezoelectric actuators can move up or down in steps of 500 nm, Fig. 3a. However, this resolution is affected when the milling machine is running. We characterized the accuracy of our platform by milling microchannels on an acrylic plate and measured their depth with a white-light interferometer. Fig. 3b shows a representative image of these measurements. A plot of the measured depth as a function of the actuator excitation voltage is shown in Fig. 3c. This data is fitted to a straight line and its equation parameters are fed into our LabVIEW program that automatically adjusts the excitation voltage to get the desired depth. Using the least squares adjustment, we found that the confident range of the vertical positioning of our platform is of the order of ±1.5 μm (±2σ, where σ is the standard deviation which is ≈0.75 μm). In contrast, the accuracy of most conventional milling machines is limited to steps of 10 μm, Fig. 3d.

After machining the microchannels and exposing them to chloroform vapor, the roughness of the channels was 130 nm, four times less than what has been reported.[6] The chloroform vapor solubilizes and polishes the acrylic surfaces[28] but also helps with the bonding of the acrylic plates. Interestingly, the walls of the microchannels are straight (Fig. 3b), indicating that our platform is immune to the vibrations generated during machining.

Device bonding

Although our platform allows excavating channels less than 10 microns in depth, this method would not be useful if it was not accompanied by a bonding strategy that does not deform the microchannels when bonding them to another layer. Although our bonding protocol uses temperatures close to acrylic's glass transition temperature (100–122 °C),[29] it does not cause any deformations as can be appreciated from the cross-sectional photographs of two channels (7 and 15 μm in depth) shown in Fig. 3(e), before and after bonding. These results underline the efficiency of our bonding protocol to smoothen the surface roughness of the microchannels and to seal them without any apparent deformation.

The total time to produce a device, from loading the design into the milling machine, milling it, and bonding it, takes on average 40 min. This is 8 hours faster than soft lithography, one of the most popular techniques for manufacturing microdevices with similar size structures. Nevertheless, this technique is still limited by the size of the drill bit diameter in the *XY* plane.

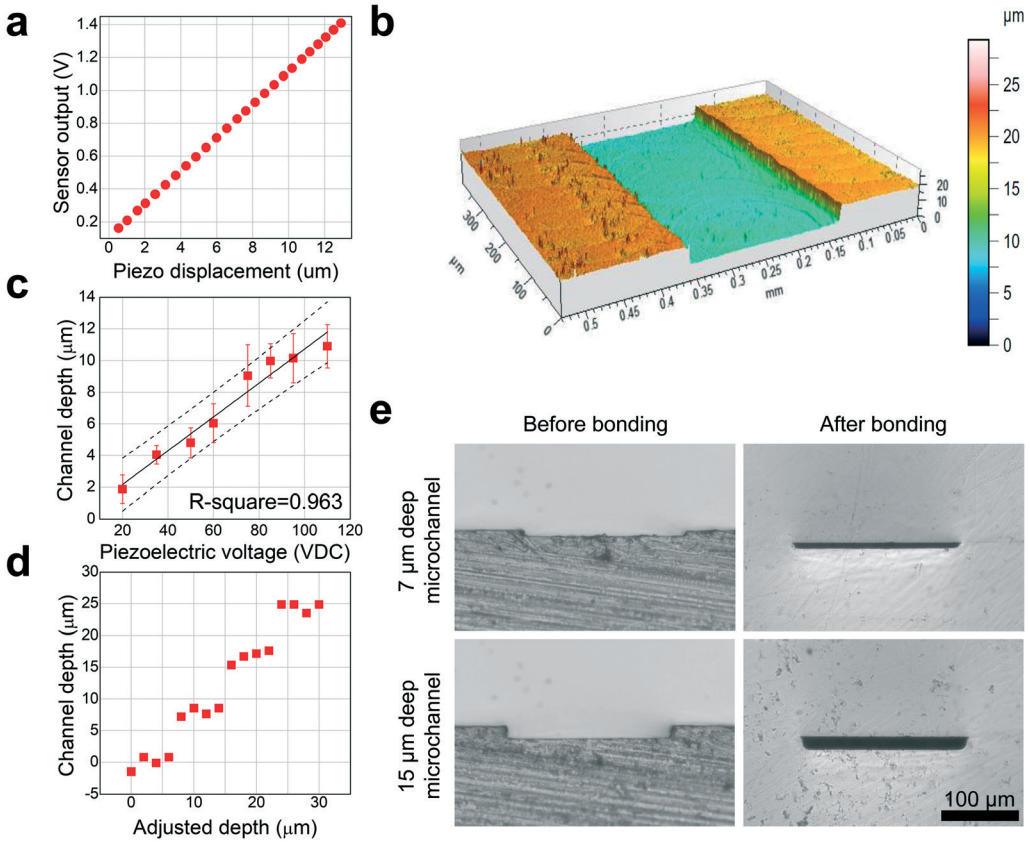

Fig. 3 (a) Voltage output readings of the actuator sensors as a function of the actuators' displacement. (b) Surface profile generated by a white-light interferometer from a typical channel of 10 μm depth. (c) Depth of machined channels using our platform as a function of the excitation voltages. The straight solid line is a linear fit to the data, and dotted lines delimit the confident bands defined by twice the standard deviation: ±1.5 μm. (d) Depths of channels machined with a regular milling machine. (e) 200 μm wide microfluidic channels of 7 μm and 15 μm depth, before and after being bonded.

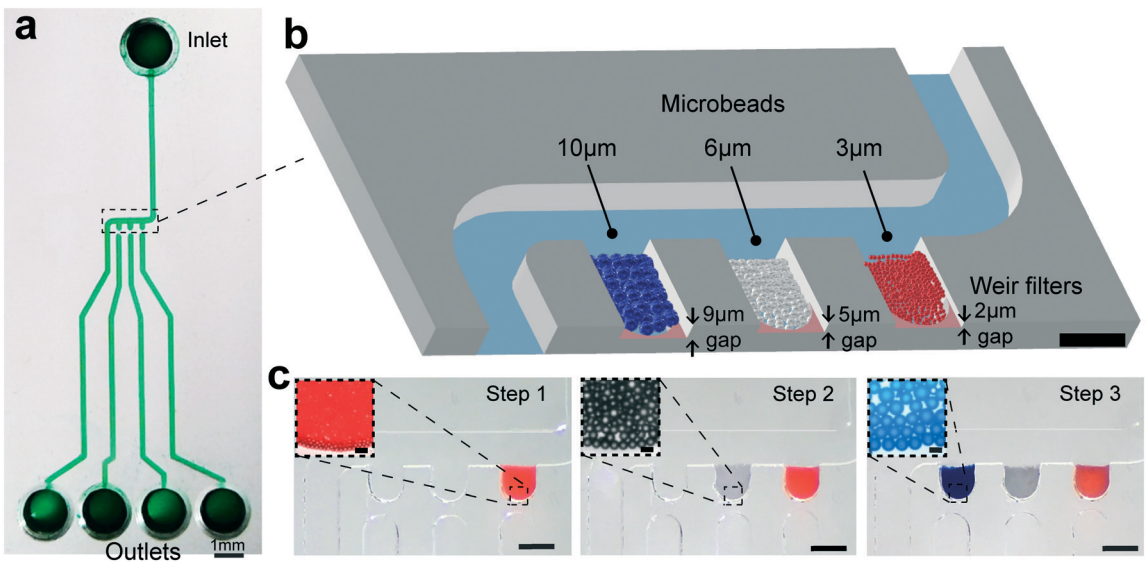

Fig. 4 (a) Top-view photograph of a device used for the parallel packing of microparticles of different sizes. (b) 3D rendering of the three traps showing how beads of different sizes are packed. (c) Microbeads are introduced in sequence with 3 μm microparticles being the first and captured by the 2 μm restriction. Next, 6 μm microparticles are flowed and captured in the 5 μm weir. Finally, the 10 μm microparticles are captured by the 9 μm restriction. All scale bars are 200 μm, except for the insets which are 10 μm.

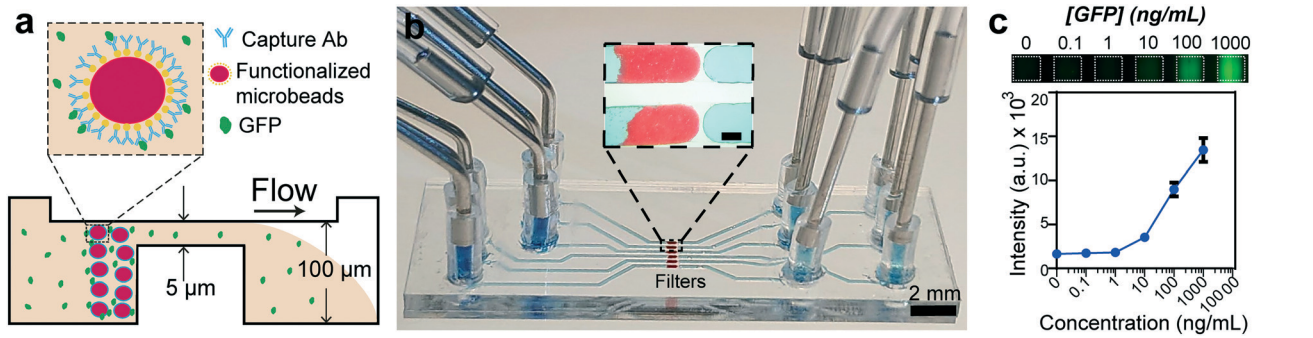

Fig. 5 (a) Schematic view of the microfluidic device to perform an immunoassay. The microbeads coated with anti-GFP antibodies bind antigens in the sample that flows through the device. (b) Photograph of the microfluidic device with a closeup to filter sections. Scale bar, 100 μm. (c) Top, fluorescence micrographs of the filters with increasing concentration of GFP. The bottom graph shows the fluorescence intensity as a function of the GFP concentration.

Fabrication of weir structures

To demonstrate the utility of our platform, we fabricated devices with embedded weir filters[30] to trap and pack microbeads, as they have several applications in chromatography. Although these weir filters have been built before using soft lithography or hot embossing, to the best of our knowledge, fabricating such fine structures with a regular desktop milling machine has not been demonstrated.

The device consists of a main channel that branches out into four parallel channels, Fig. 4a. All the channels are 200 μm wide and 100 μm deep. Three of the branched channels have weir filters where the depth of the channel decreases from 100 μm to 2, 5 and 9 μm (Fig. 4b). As microbeads flow through the channels, beads smaller than the weir height would pass unperturbed through the weir, while beads larger than or equal to the weir height will get trapped and start accumulating at the filter. For example, in Fig. 4c (step 1), 3 μm beads accumulate in the 2 μm weir filter, as is the case for 6 μm beads in the 5 μm filter (step 2) and the 10 μm beads in the 9 μm filter (step 3). One caveat is that the microbeads must be introduced from smaller to larger sizes; otherwise, if large particles flow first, they accumulate in all the weir filters.

Our device offers potential alternatives to filtering or chromatography applications where it is important to control the porosity of the channel, which in our case is possible by tuning the weir filter height, the diameter of the beads, and the density of the bead packing.[21] For example, it would be possible to redesign the device shown in Fig. 4 to connect the different filters in series instead of in parallel. Such a device could serve as a liquid chromatography column, in which each section (filter) of the column would have particular separation properties.

Bead-based immunoassay on a chip

An immunoassay is a biochemical method that relies on the interaction of an antibody and antigen to detect and quantify analytes (*e.g.* proteins, lipids, and nucleic acids) in a biological fluid (serum, urine, *etc.*).[22] Immunoassays are widely employed in the diagnosis of different diseases such as HIV, cancer, and tuberculosis, among others.[31,32] To demonstrate the suitability of our microfluidic device in diagnostics, we performed a proof-of-concept immunoassay using green fluorescent protein (GFP). GFP allowed us to assess in real-time the binding of proteins to antibodies using time-lapse fluorescence microscopy. Using similar weir filters and traps as described in the previous section, we engineered a device to perform up to 6 immunoassays in parallel. The device contains 6 inlets, 6 outlets and 6 channels (200 μm wide, 100 μm deep), each with a weir filter (5 μm deep) in the middle of the channel (Fig. 5a and b). Each channel was filled with 6.7 μm polystyrene beads functionalized with antibodies against green fluorescent protein (GFP).

After forming the columns of functionalized microbeads, six different concentrations of GFP ranging from 0 to 1000 ng mL^{-1} were injected to separate channels for 10 min. Fluorescence micrographs acquired from sections of each filter show that the fluorescence intensity increases as a function of concentration in an exponential fashion with a limit of detection of 1 ng mL^{-1}, Fig. 5c. This application demonstrates the utility of our 3D-printed fixture to fabricate acrylic devices in a short time frame with resolutions similar to lithography.

Conclusions

We have presented a simple and low-cost fixture to improve the resolution and accuracy of the vertical positioning of conventional milling machines to fabricate microfluidic devices. Our mechatronic fixture consists of three piezoelectric actuators assembled inside a plastic housing made with a 3D printer. Importantly, it has the ability to include flexible hinges that elevate the platform, without the need to resort to springs or other mechanical structures. Simulations informed us that the hinges can deform without suffering any mechanical or structural damage, which was further corroborated by the hundreds of times the fixture has

been used in our labs to fabricate microfluidic devices. We demonstrated that our fixture allowed us to produce thermoplastic microfluidic channels with controlled depth sizes (3, 6 and 10 μm) without any deformation during their fabrication or when sealed them to another acrylic piece. We also showed how to selectively capture beads of different sizes in these weir filters. Finally, we implemented a bead-based microfluidic immunoassay exploiting these weir structures. The use of this microfluidic system can have different applications, for example in creating columns for chromatography,[20,21] separation of cells of different sizes[33] and environmental or analytical chemistry applications.[34]

Overall, we have demonstrated a simple and robust positioner fixture for increasing the resolution of conventional milling machines. The simplicity with which our 3D printing fixture is fabricated and assembled, and its low cost open the possibility for research laboratories to adapt it very quickly for conventional milling, but also for other applications that may require some of form of positioning.

Conflicts of interest

There are no conflicts to declare.

Acknowledgements

JLGC acknowledges support from Mexico's CONACYT Grants ERC-297690, and CB-286368, and a Cinvestav Grant No. SEP FIDSC2018/104. GACR acknowledges support from Mexico's CONACYT Grant Fronteras de la Ciencia 2015-2/1178. GACR acknowledges laboratory NIMBE-Université Paris-Saclay, more specifically F. Malloggi laboratory, where some of this work was performed during his sabbatical stay.

References

1 E. K. Sackmann, A. L. Fulton and D. J. Beebe, *Nature*, 2014, **507**, 181.
2 P. E. Guevara-Pantoja, R. J. Jiménez-Valdés, J. L. García-Cordero and G. A. Caballero-Robledo, *Lab Chip*, 2018, **18**, 662–669.
3 E. Berthier, E. W. K. Young and D. Beebe, *Lab Chip*, 2012, **12**, 1224–1237.
4 H. Shadpour, H. Musyimi, J. Chen and S. A. Soper, *J. Chromatogr. A*, 2006, **1111**, 238–251.
5 P.-C. Chen, C.-W. Pan, W.-C. Lee and K.-M. Li, *Int. J. Adv. Des. Manuf. Technol.*, 2014, **71**, 1623–1630.
6 D. J. Guckenberger, T. E. de Groot, A. M. D. Wan, D. J. Beebe and E. W. K. Young, *Lab Chip*, 2015, **15**, 2364–2378.
7 C. D. Chin, V. Linder and S. K. Sia, *Lab Chip*, 2012, **12**, 2118–2134.
8 A. K. Au, W. Huynh, L. F. Horowitz and A. Folch, *Angew. Chem., Int. Ed.*, 2016, **55**, 3862–3881.
9 D. Patko, Z. Mártonfalvi, B. Kovacs, F. Vonderviszt, M. Kellermayer and R. Horvath, *Sens. Actuators, B*, 2014, **196**, 352–356.
10 J. Jiang, J. Zhan, W. Yue, M. Yang, C. Yi and C.-W. Li, *RSC Adv.*, 2015, **5**, 36036–36043.
11 Y. Sun, Y. C. Kwok and N.-T. Nguyen, *J. Micromech. Microeng.*, 2006, **16**, 1681.
12 C. W. Tsao, L. Hromada, J. Liu, P. Kumar and D. L. DeVoe, *Lab Chip*, 2007, **7**, 499–505.
13 H. Becker and C. Gärtner, *Anal. Bioanal. Chem.*, 2008, **390**, 89–111.
14 P. E. Guevara-Pantoja, R. J. Jiménez-Valdés, J. L. García-Cordero and G. A. Caballero-Robledo, *Lab Chip*, 2018, **18**, 662–669.
15 L. Zhu, Q. Zhang, H. Feng, S. Ang, F. S. Chau and W.-T. Liu, *Lab Chip*, 2004, **4**, 337–341.
16 J. S. Shim, A. W. Browne and C. H. Ahn, *Biomed. Microdevices*, 2010, **12**, 949–957.
17 X. Chen, C. C. Liu and H. Li, others, *Sens. Actuators, B*, 2008, **130**, 216–221.
18 K. Sato, M. Tokeshi, T. Odake, H. Kimura, T. Ooi, M. Nakao and T. Kitamori, *Anal. Chem.*, 2000, **72**, 1144–1147.
19 H. W. Hou, A. A. S. Bhagat, W. C. Lee, S. Huang, J. Han and C. T. Lim, *Micromachines*, 2011, **2**, 319–343.
20 R. D. Oleschuk, L. L. Shultz-Lockyear, Y. Ning and D. J. Harrison, *Anal. Chem.*, 2000, **72**, 585–590.
21 P. E. Guevara-Pantoja and G. A. Caballero-Robledo, *RSC Adv.*, 2015, **5**, 24635–24639.
22 A. H. C. Ng, U. Uddayasankar and A. R. Wheeler, *Anal. Bioanal. Chem.*, 2010, **397**, 991–1007.
23 P. E. Guevara-Pantoja, M. Sánchez-Domínguez and G. A. Caballero-Robledo, *Biomicrofluidics*, 2020, **14**, 014111.
24 X. Zhou, S.-J. Hsieh and C.-C. Ting, *Virtual Phys. Prototyp.*, 2018, **13**, 177–190.
25 T. Letcher and M. Waytashek, in *Volume 2A: Advanced Manufacturing*, American Society of Mechanical Engineers, 2014.
26 Y. Song, Y. Li, W. Song, K. Yee, K.-Y. Lee and V. L. Tagarielli, *Mater. Des.*, 2017, **123**, 154–164.
27 S. Farah and D. G. Anderson, *Adv. Drug Delivery Rev.*, 2016, **107**, 367–392.
28 I. R. G. Ogilvie, V. J. Sieben, C. F. A. Floquet, R. Zmijan, M. C. Mowlem and H. Morgan, *J. Micromech. Microeng.*, 2010, **20**, 65016.
29 C.-W. Tsao and D. L. DeVoe, *Microfluid. Nanofluid.*, 2009, **6**, 1–16.
30 H. M. Ji, V. Samper, Y. Chen, C. K. Heng, T. M. Lim and L. Yobas, *Biomed. Microdevices*, 2008, **10**, 251–257.
31 J. F. Rusling, C. V. Kumar, J. S. Gutkind and V. Patel, *Analyst*, 2010, **135**, 2496.
32 P. Yager, G. J. Domingo and J. Gerdes, *Annu. Rev. Biomed. Eng.*, 2008, **10**, 107–144.
33 C. van Rijn, W. Nijdam and M. Elwenspoek, in *Proceedings of 18th Annual International Conference of the IEEE Engineering in Medicine and Biology Society*, 1996, vol. 1, pp. 256–257.
34 H. Andersson, W. van der Wijngaart and G. Stemme, *Electrophoresis*, 2001, **22**, 249–257.

